The Astrophysical Journal, 749:40 (14pp), 2012 April 10 doi:10.1088/0004-637X/749/1/40

CORONAL CELLS

N. R. Sheeley, Jr. and H. P. Warren
Space Science Division, Naval Research Laboratory, Washington, DC 20375-5352, USA; neil.sheeley@nrl.navy.mil, harry.warren@nrl.navy.mil
Received 2012 January 6; accepted 2012 February 1; published 2012 March 20

ABSTRACT

We have recently noticed cellular features in Fe XII 193 Å images of the 1.2 MK corona. They occur in regions bounded by a coronal hole and a filament channel, and are centered on flux elements of the photospheric magnetic network. Like their neighboring coronal holes, these regions have minority-polarity flux that is ∼0.1–0.3 times their flux of majority polarity. Consequently, the minority-polarity flux is "grabbed" by the majority-polarity flux to form low-lying loops, and the remainder of the network flux escapes to connect with its opposite-polarity counterpart in distant active regions of the Sun. As these regions are carried toward the limb by solar rotation, the cells disappear and are replaced by linear plumes projecting toward the limb. In simultaneous views from the *Solar Terrestrial Relations Observatory* and *Solar Dynamics Observatory* spacecraft, these plumes project in opposite directions, extending away from the coronal hole in one view and toward the hole in the other view, suggesting that they are sky-plane projections of the same radial structures. We conclude that these regions are composed of closely spaced radial plumes, extending upward like candles on a birthday cake and visible as cells when seen from above. We suppose that a coronal hole has this same discrete, cellular magnetic structure, but that it is not seen until the encroachment of opposite-polarity flux closes part or all of the hole.

Key words: Sun: corona – Sun: filaments, prominences – Sun: magnetic topology – Sun: surface magnetism – Sun: UV radiation

Online-only material: color figures

1. INTRODUCTION

This study began when one of us (N.R.S.) made a routine visit to the Solar Data Analysis Center (SDAC) Web site[1] of the NASA Goddard Spaceflight Center. On that day, an Fe XII 193 Å solar image, obtained with the Atmospheric Imaging Assembly (AIA) on the *Solar Dynamics Observatory* (*SDO*; Lemen et al. 2012) showed a large region of cellular features near the center of the disk. The cells looked remarkably like photospheric granules, with bright centers separated by narrow dark lanes. However, these coronal cells were much larger than photospheric granules and had sizes comparable to the ∼30,000 km diameters of supergranules (Simon & Leighton 1964). Although we were familiar with the ∼30,000 km grid that appears on images obtained in lower temperature lines of the chromosphere and transition region (i.e., below the ∼0.6 MK temperature of Ne VIII), we could not recall ever having seen cells in images obtained with emission lines formed at temperatures ∼1 MK (Feldman et al. 1999, 2000).

Consequently, we decided to determine the properties of these coronal cells. We combined AIA Fe XII 193 Å images with photospheric magnetograms, obtained with the Helioseismic and Magnetic Imager (HMI) on *SDO*, to determine the magnetic properties of these cells (Schou et al. 2012). We used the Extreme-Ultraviolet Imaging Spectrometer (EIS) on the *Hinode* spacecraft to determine the temperatures and line-of-sight Doppler velocities of these cells (Culhane et al. 2007; Doschek et al. 2007). We combined AIA Fe XII 193 Å images with Fe XII 195 Å images, obtained with the Extreme Ultraviolet Imagers (EUVI) on the *Solar Terrestrial Relations Observatory* (*STEREO*), to determine the center-to-limb variation, the three-dimensional structure, and the lifetimes of the cells (Howard et al. 2008). And we used Fe XII 195 Å images, obtained with the Extreme Ultraviolet Imaging Telescope (EIT) on the *Solar and Heliospheric Observatory* (*SOHO*), to look for cellular patterns during the previous sunspot cycle (Domingo et al. 1995; Delaboudinière et al. 1995). This paper presents our findings.

As we shall see in the next section, the cells are radially extending plumes that extend outward from photospheric network elements like candles on a birthday cake. The cells are most visible at temperatures ∼1 MK. Doppler measurements indicate that the cell centers move upward faster than their edges. Like coronal holes, their magnetic fields are dominated by a single polarity, but with a small contamination of minority-polarity flux in the internetwork regions. The cells bear an evolutionary relation to coronal holes, appearing where the holes contract and disappearing where the holes expand. Fe XII 195 Å EIT images from the *SOHO* spacecraft show numerous cellular regions during the active phase of the previous sunspot cycle, but not in the years around sunspot minimum.

We have previously seen that during the rising phase of the sunspot cycle, new-cycle active regions produce high-latitude filament channels and enhancements of intensity along the edges of the polar coronal holes, apparently when the closed loops of the active region reconnect with the open fields of the hole (Sheeley et al. 1989). Because these enhancements are bounded between the coronal holes and the filament channels, they have the same geometry as the cellular regions of this study. Consequently, we suppose that these enhancements along the boundaries of the polar holes are cellular regions whose cells would be visible if we could observe them from high latitude. This suggests that the edge enhancements and the cellular regions may have a common origin in the field-line reconnection of coronal holes.

2. OBSERVATIONS

We begin by identifying a region of coronal cells and showing where it is located relative to other coronal and photospheric

[1] http://umbra.nascom.nasa.gov/images

Report Documentation Page

Form Approved
OMB No. 0704-0188

1. REPORT DATE	2. REPORT TYPE	3. DATES COVERED
10 MAR 2012		**00-00-2012 to 00-00-2012**

4. TITLE AND SUBTITLE	5a. CONTRACT NUMBER
Coronal Cells	5b. GRANT NUMBER
	5c. PROGRAM ELEMENT NUMBER
6. AUTHOR(S)	5d. PROJECT NUMBER
	5e. TASK NUMBER
	5f. WORK UNIT NUMBER
7. PERFORMING ORGANIZATION NAME(S) AND ADDRESS(ES) **Naval Research Laboratory,Space Science Division,Washington,DC,20375-5352**	8. PERFORMING ORGANIZATION REPORT NUMBER
9. SPONSORING/MONITORING AGENCY NAME(S) AND ADDRESS(ES)	10. SPONSOR/MONITOR'S ACRONYM(S)
	11. SPONSOR/MONITOR'S REPORT NUMBER(S)

12. DISTRIBUTION/AVAILABILITY STATEMENT
Approved for public release; distribution unlimited

13. SUPPLEMENTARY NOTES

14. ABSTRACT

We have recently noticed cellular features in Fe xii 193?images of the 1.2 MK corona. They occur in regions bounded by a coronal hole and a filament channel, and are centered on flux elements of the photospheric magnetic network. Like their neighboring coronal holes, these regions have minority-polarity flux that is ∼0.1?0.3 times their flux of majority polarity. Consequently, the minority-polarity flux is ?grabbed? by the majority-polarity flux to form low-lying loops, and the remainder of the network flux escapes to connect with its opposite-polarity counterpart in distant active regions of the Sun. As these regions are carried toward the limb by solar rotation, the cells disappear and are replaced by linear plumes projecting toward the limb. In simultaneous views from the Solar Terrestrial Relations Observatory and Solar Dynamics Observatory spacecraft, these plumes project in opposite directions extending away from the coronal hole in one view and toward the hole in the other view, suggesting that they are sky-plane projections of the same radial structures. We conclude that these regions are composed of closely spaced radial plumes, extending upward like candles on a birthday cake and visible as cells when seen from above. We suppose that a coronal hole has this same discrete, cellular magnetic structure, but that it is not seen until the encroachment of opposite-polarity flux closes part or all of the hole.

15. SUBJECT TERMS

16. SECURITY CLASSIFICATION OF:			17. LIMITATION OF ABSTRACT	18. NUMBER OF PAGES	19a. NAME OF RESPONSIBLE PERSON
a. REPORT **unclassified**	b. ABSTRACT **unclassified**	c. THIS PAGE **unclassified**	**Same as Report (SAR)**	**14**	

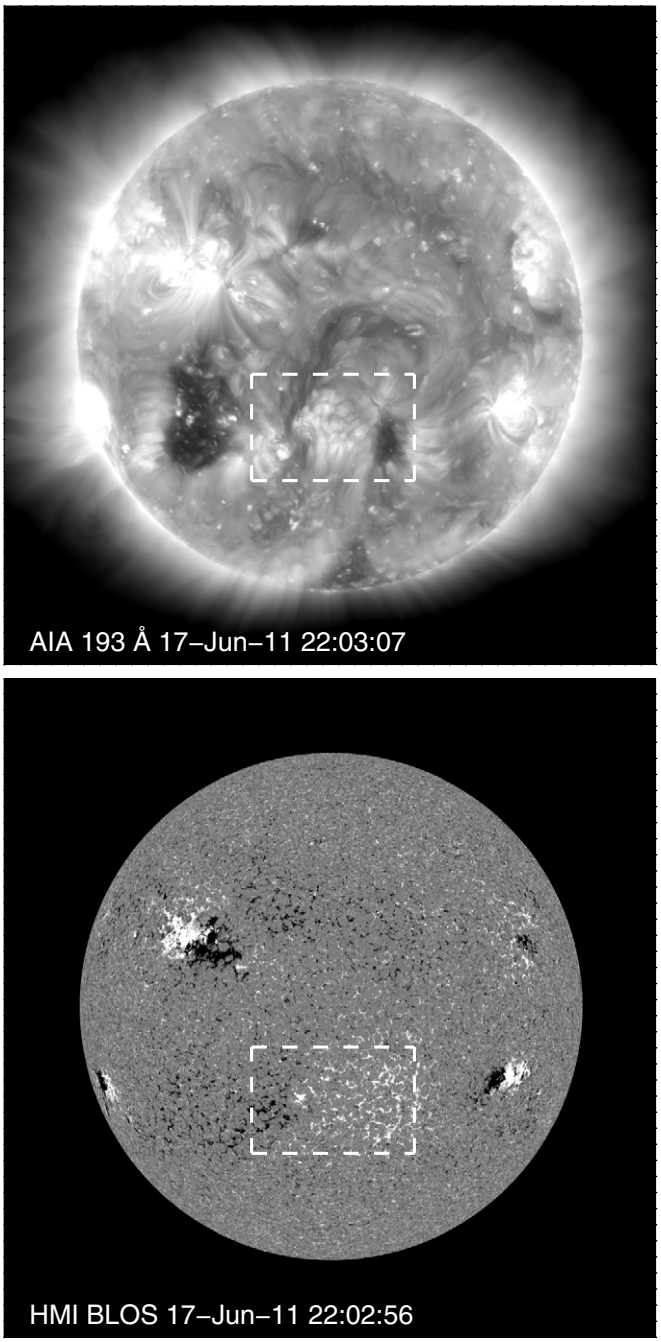

Figure 1. AIA 193 Å image (top) and an HMI magnetogram (bottom) on 2011 June 17, showing coronal cells in a magnetic region of positive (white) network bounded by a small coronal hole (right) and a filament channel/magnetic neutral line (left). The box refers to the region shown in Figure 2.

magnetic features. In the Fe XII 193 Å image in the top panel of Figure 1, the cellular region is located at the central meridian in the southern hemisphere between a filament channel winding along its east (left) side and a small coronal hole on its west (right) side. We have enclosed this area in a dashed box to relate it to the photospheric field shown in the bottom panel of the figure. As one can see, the cells and the coronal hole lie in a large region dominated by a fragmentary network of positive (white) magnetic polarity. The filament channel winds along the "neutral line" that separates this positive-polarity region from the negative (black)-polarity region to its east.

Figure 2 shows a blow-up of the boxed region in Figure 1. In each panel, the image has been enhanced by averaging all of the available high time resolution *SDO* images obtained during a 6 minute interval. Numerous cells, separated by narrow dark lanes, are visible in the Fe XII coronal image, and corresponding positive-polarity elements of flux are visible in the magnetogram. The superposition of these two images reveals that the coronal cells are centered on the positive-polarity network elements, not between these elements where the horizontal supergranular flows are located. This fact, that the coronal intensity cells are offset from the supergranular cells, is an important distinction that will affect our interpretation in the next section.

We have made magnetic measurements of the region of cells and the coronal hole on its western boundary. In each case, we measured a noise level by fitting the core of the flux histogram with a Gaussian of half-width at half-maximum of 4.5 G, and then determined the relative amounts of positive and negative flux when this Gaussian "noise" was subtracted from the histogram. In this case, the ratio of minority- to majority-polarity flux was 0.10 for the cellular region and 0.07 for the coronal hole. (The numbers were slightly larger—0.14 and 0.11, respectively—if we simply limited the histograms to fields greater than 4.5 G without subtracting the Gaussian.) The main point is that the cellular region and its adjacent coronal hole were both unipolar, but with a minority-polarity component only 0.1 that of the majority polarity. This proportion of minority-polarity flux is comparable to what we have measured for other cellular regions, as we shall show later in this section.

The magnetic field lines in Figure 3 suggest how the unbalanced flux in the cellular region is connected to its opposite-polarity counterparts in other regions of the Sun. Most of this positive-polarity region is linked by orange closed loops to negative-polarity flux across the neutral line and to the negative pole of the large active region in the northeast. But in the western part of the positive-polarity region, blue lines extend outward, indicating the open magnetic fields of the coronal hole. In general, this is the configuration that occurs where coronal cells are located—open (or nearly open) flux on one side and closed flux extending across a magnetic neutral line on the other side.

Next, we consider how this cellular region changes its appearance as it is carried across the disk by solar rotation. Figures 4 and 5 show the transition, first as seen from *STEREO-B* (located 93° east of Earth at this time) and *SDO* (located at the L1 point on the Earth–Sun line), and then from *SDO* and *STEREO-A* (located 96° west of Earth).

As shown in the upper left panel of Figure 4, the cells were visible from *STEREO-B* on June 10 when the region was well on the disk. By June 13, most of the cells were replaced by plume-like features projecting westward toward the limb (as shown in the lower left panel). At approximately the same time, those same plumes were visible from *SDO*, but projecting eastward in the opposite direction (as shown in the lower right panel). By June 17, the region had moved well onto the disk as seen from *SDO*, and the cells were again visible (as shown in the upper right panel). This suggests that we are observing the sky-plane projections of plume-like features extending radially outward from the Sun, and that these features look like cells when observed from above.

Figure 5 shows that the same result is obtained when going from *SDO* to *STEREO-A*. The cellular pattern that was visible near disk center from *SDO* changed to a pattern of inclined

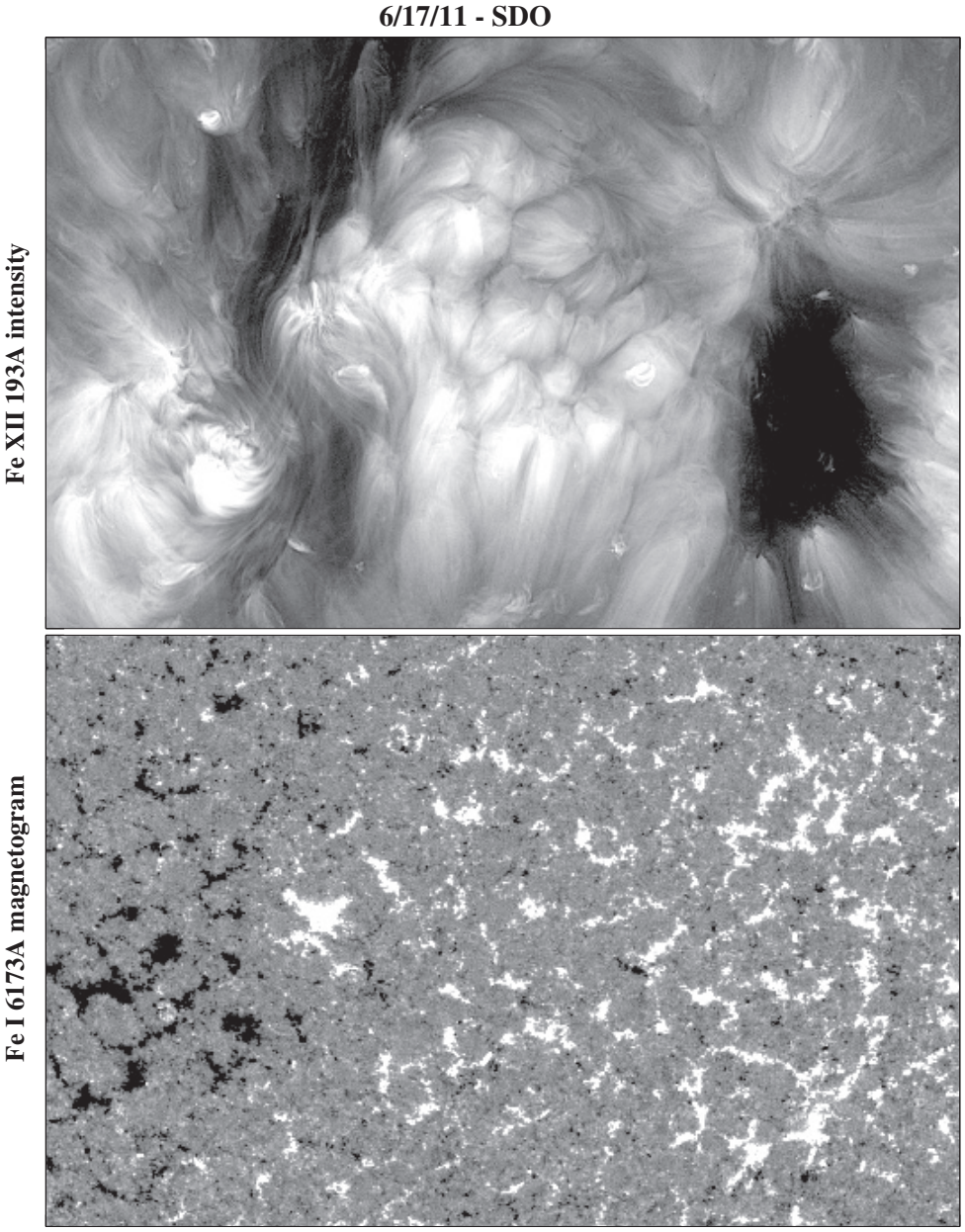

Figure 2. Blow-up of the regions within the dotted boxes of Figure 1, showing the Fe XII cells between the filament channel to the left and the coronal hole to the right. A detailed comparison between the Fe XII image and the photospheric magnetogram indicates that the cells are centered on the positive (white)-polarity network fragments.

rays projecting toward the west limb 4 days later. The nearly simultaneous view from *STEREO-A* on June 21 showed these same features, projecting eastward in the opposite direction (as shown by the arrows in the lower panels of Figure 5). Four days later, when the region had moved well onto the disk, the cells were visible from *STEREO-A* (upper right panel).

In Figure 6, we examine another cellular region, this time near the central meridian on 2011 September 8, as seen from *SDO*. It is the slanted pattern located between the northwest boundary of a large coronal hole and a filament channel to its west. The area within the dotted box is shown in Figure 7. For this region, the majority polarity was negative (black), and the ratio of minority- to majority-polarity flux was 0.16 for both the cellular pattern and its adjacent coronal hole. Also, like our first example, as solar rotation carried the region toward the limb, the cells changed into plumes projecting toward the limb. Figure 8 illustrates this fact, showing a plume leaning westward away from the coronal hole boundary as seen from *STEREO-B*, and eastward over the hole as seen in the nearly simultaneous image from *SDO*.

Our third example is shown in Figure 9. Here, the cellular pattern is bounded on the west by a filament channel, but on the east by large-scale structures adjacent to a coronal hole. These structures were formed during September 1–3 when a large coronal hole at this location closed down. As in the previous examples, the dotted box identifies the area shown in the next figure. Magnetic measurements on September 20 give a minority- to majority-polarity flux ratio of 0.30 for the region of cells. On August 24, the coronal hole at this location had a minority- to majority-polarity flux ration of 0.40. On the other side of the neutral line, the ratio was $\sim$0.002 in the positive-polarity part of the active region, indicating a very

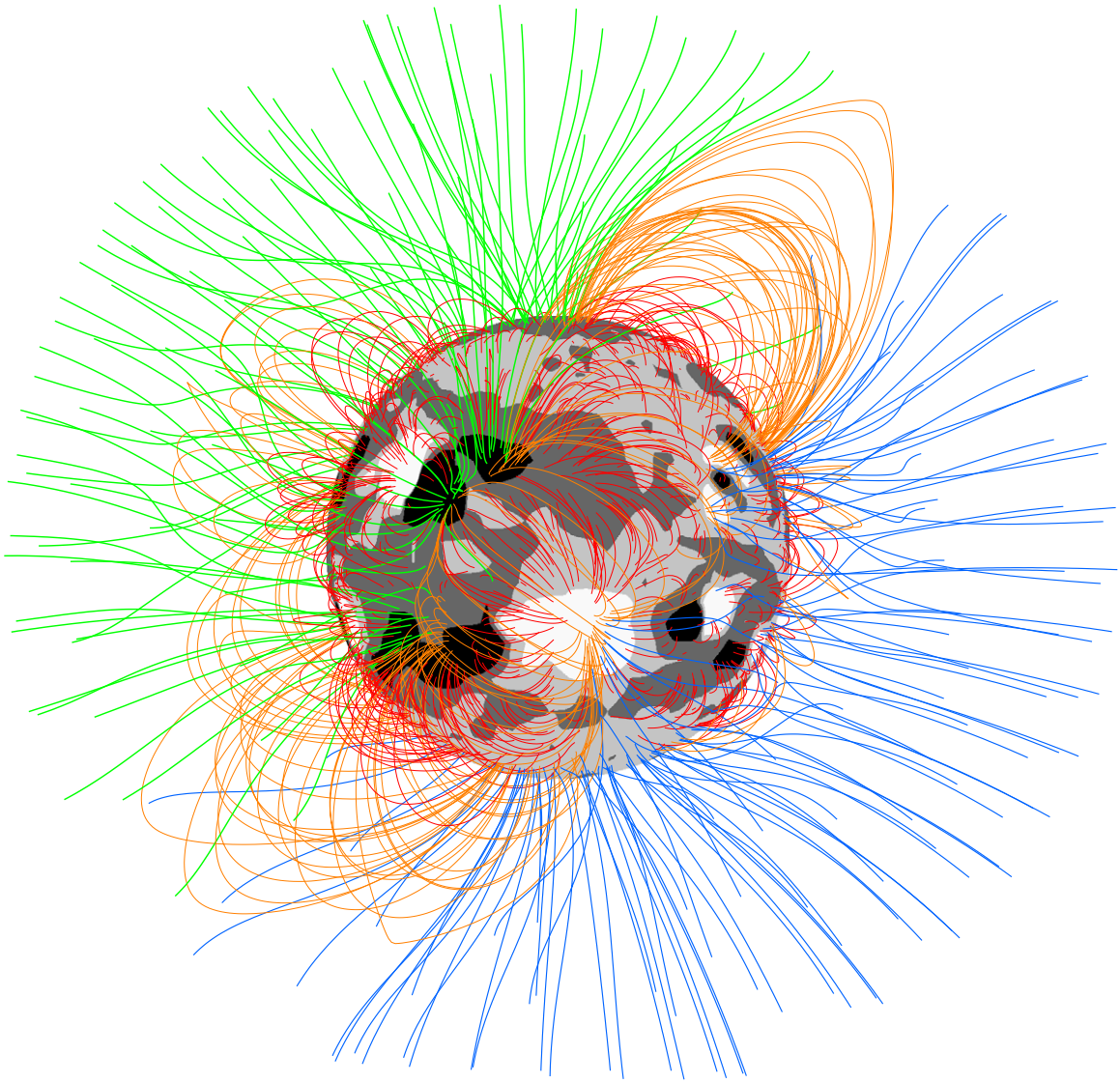

Figure 3. Magnetic field lines, derived from the National Solar Observatory (NSO) Carrington map for rotation 2111 using the Naval Research Laboratory (NRL) source-surface potential field program (Wang & Sheeley 1992), and showing the field-line configuration visible from Earth on 2011 June 17 when the images in Figure 1 were taken. Closed field lines (orange) arch eastward and northward from the positive (white)-polarity region near the central meridian, linking its cells to negative flux in active regions. Open (blue) field lines extend outward from a coronal hole in the right side of this region.

(A color version of this figure is available in the online journal.)

high degree of unipolarity. By comparison, a quiet region on August 24 had a ratio of 0.94, indicating nearly equal amounts of positive and negative flux. Our point is that the cellular regions have fields that are similar to the fields in their adjacent coronal holes—unipolar, but containing a noticeable amount of minority-polarity flux (0.1–0.3 times the amount of majority-polarity flux).

In Figure 10, we have included an image obtained with the Fe IX/X 171 Å filter whose temperature of formation is about 0.6 MK. At this relatively low temperature, the structures no longer look like individual cells separated by narrow dark boundaries. Instead, they appear as a collection of small-scale fibrils attached to the network of magnetic flux concentrations like elements of the chromosphere. Figure 11 shows the evolution of this cellular pattern when it was most visible during September and October. During this relatively long time, the pattern of cells became appreciably sheared by differential rotation, but the narrow boundaries between the cells remain sharply defined.

In Figure 12, we compare an AIA 193 Å image with a sequence of spectrally resolved images of the same solar area, obtained with the EIS instrument on the *Hinode* spacecraft on 2011 November 15. These EIS images were constructed from a temporal sequence of spectra obtained by scanning across the observed spatial region during the 3 hr 24 minute interval 10:55–14:19 UT. In the AIA image (upper left panel), the cells are visible along the southwest (lower right) boundary of the coronal hole in the center of the region. Looking along the sequence of increasing temperature, we see that the cells are most visible in the lines of Fe XI and Fe XII, corresponding to a temperature ∼1.2 MK. We have also observed coronal cells in images obtained with the AIA 335 Å filter. The sequence of spectrally resolved EIS images suggests the visibility of the cells in the AIA 335 Å images is due to the contribution of ∼1 MK

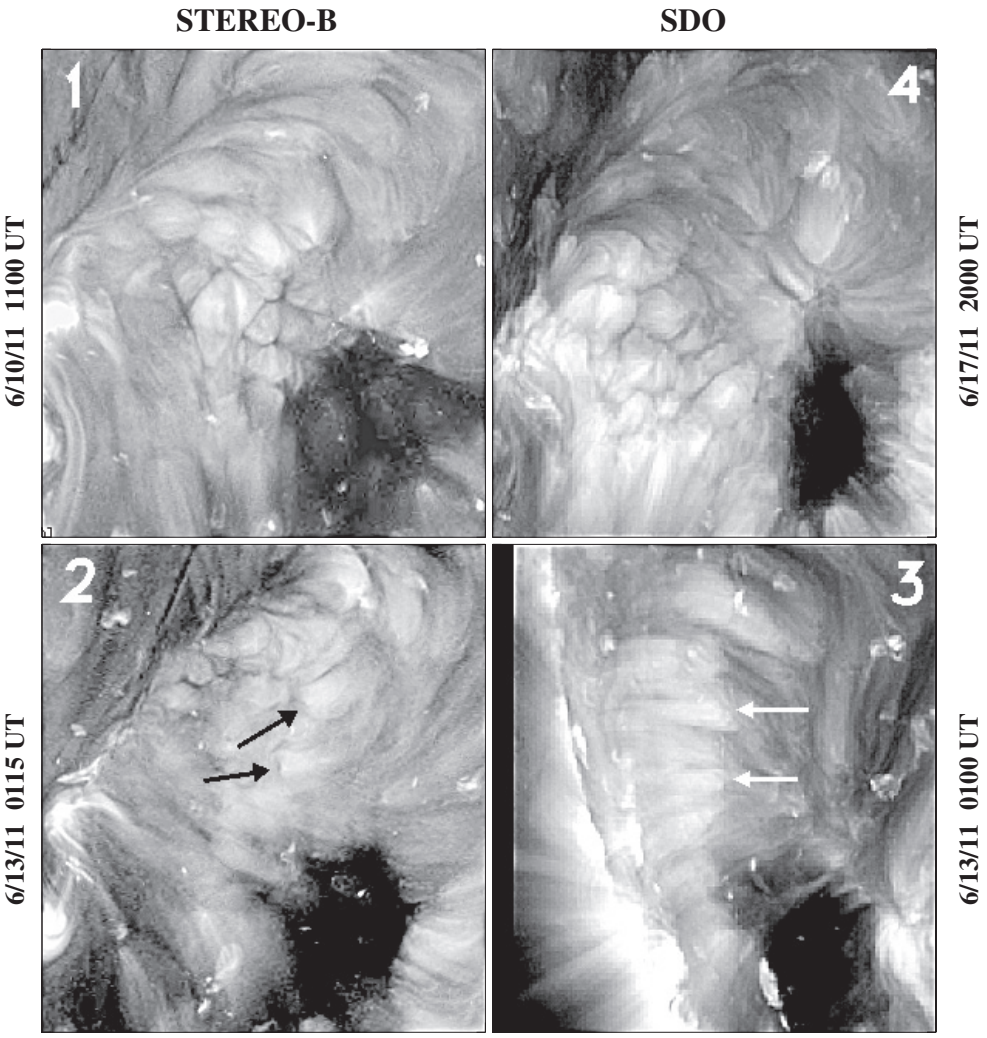

Figure 4. Progressing counterclockwise from the upper left, the first image shows the cell pattern near the central meridian as seen from the *STEREO-B* spacecraft (located 93° east of Earth), the second image provides an oblique view of the region 2.5 days later when it was closer to the west limb, the third image provides a simultaneous view of the same features from the *SDO* spacecraft (located at the L1 point on the Earth–Sun line), and the fourth image provides another head-on view of the cells when they are near central meridian as seen from *SDO*. In the simultaneous oblique views, the arrows indicate identical features projecting in opposite directions as if they were extending radially outward from the Sun.

lines in the relatively wider bandpass of the filter, not the result of emission in the Fe XVI 335 Å line whose temperature is ∼2.5 MK.

Because these EIS images were constructed from a sequence of spectral line profiles, we can use these same line profiles to construct a Dopplergram of this region, showing the line-of-sight speed of the plasma relative to an arbitrary zero point (Young et al. 2012; Warren et al. 2011). The middle panel of Figure 13 contains the resulting Fe XII 193 Å Dopplergram. Upward and downward motions (relative to an arbitrary zero point) are indicated by blue and red shading, respectively. For comparison, the Fe XII intensity field is shown in the left panel and the intensity contours are superimposed on the Dopplergram in the right panel. It is easy to see that narrow bands of red color wind along the cell boundaries, indicating downward motions of ∼20 km s^{-1} relative to the cell centers. Because the zero point of motion is not known, it is equivalent to say that the upward motions are ∼20 km s^{-1} faster in the centers of the cells than at their boundaries.

Finally, we note that cells are visible in Fe XII 195 Å images obtained with the EIT instrument on *SOHO*. Figure 14 shows such an image on 2000 December 6, near the peak of the previous sunspot cycle. As in our more recent examples, the cellular region is bounded by a coronal hole (left) and a filament channel (right). Because the cells tend to be most visible near disk center, we have been able to use Carrington maps of Fe XII 195 Å intensity to find numerous additional examples during times of high solar activity in sunspot cycle 23.

3. SUMMARY AND DISCUSSION

In the previous section, we have identified cellular patterns that lie in unipolar regions between coronal holes and filament channels. The cells are centered on the enhanced network elements of the large-scale region, not on the internetwork areas where the horizontal motions of the supergranulation occur. Thus, the coronal cells have the spatial scale of the magnetic network, but they do not coincide with the supergranular cells.

Spectral observations from the EIS instrument on the *Hinode* spacecraft indicate that these cells are visible in emission lines formed at approximately 1 MK. And like the adjacent coronal holes, the cellular regions have an appreciable contribution of

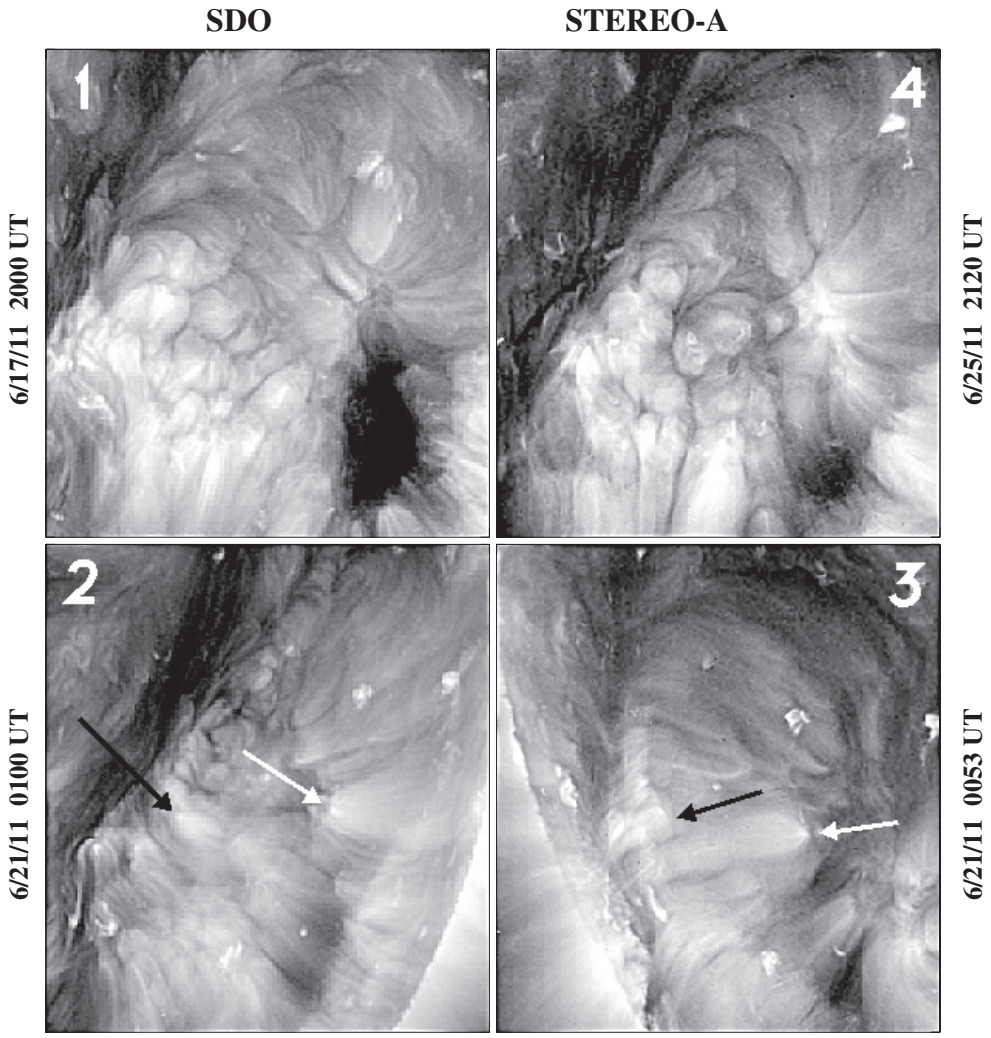

Figure 5. Same as Figure 4, except beginning with *SDO* and ending with *STEREO-A* (located 96° west of Earth). Again, the cells seen near central meridian change into plumes when seen toward the limb. Their oppositely directed projections in the simultaneous, nearly perpendicular views suggest that these plumes are directed radially outward from the Sun, and appear as cells only when seen from above.

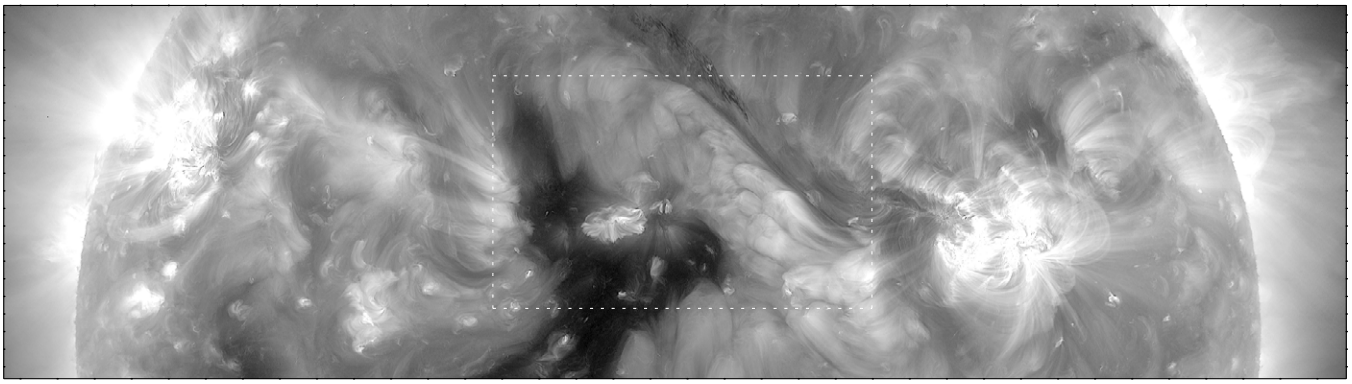

Figure 6. Fe XII 193 Å image of the Sun on 2011 September 8, when a slanted region of coronal cells is located between the northern edge of a coronal hole and the southern edge of a filament channel. The box refers to the region shown in Figure 7.

minority-polarity flux with a ratio of minority- to majority-polarity flux in the range 0.1–0.3. Dopplergrams with the EIS Fe XII 193 Å line show that the plasma at the centers of the cells moves upward of ∼20 km s^{-1} faster than the plasma at the cell boundaries. Equivalently, the material at the cell boundaries moves downward at speeds ∼10 km s^{-1} relative to the average speed in the field of view.

As solar rotation carries these regions away from disk center, the cells are transformed into elongated features that project toward the limb. Nearly simultaneous observations from the *STEREO* and *SDO* spacecraft show identical features projecting in opposite directions against the sky. Evidently, we are observing the sky-plane projection of radially extending features that are visible as cells when seen from above.

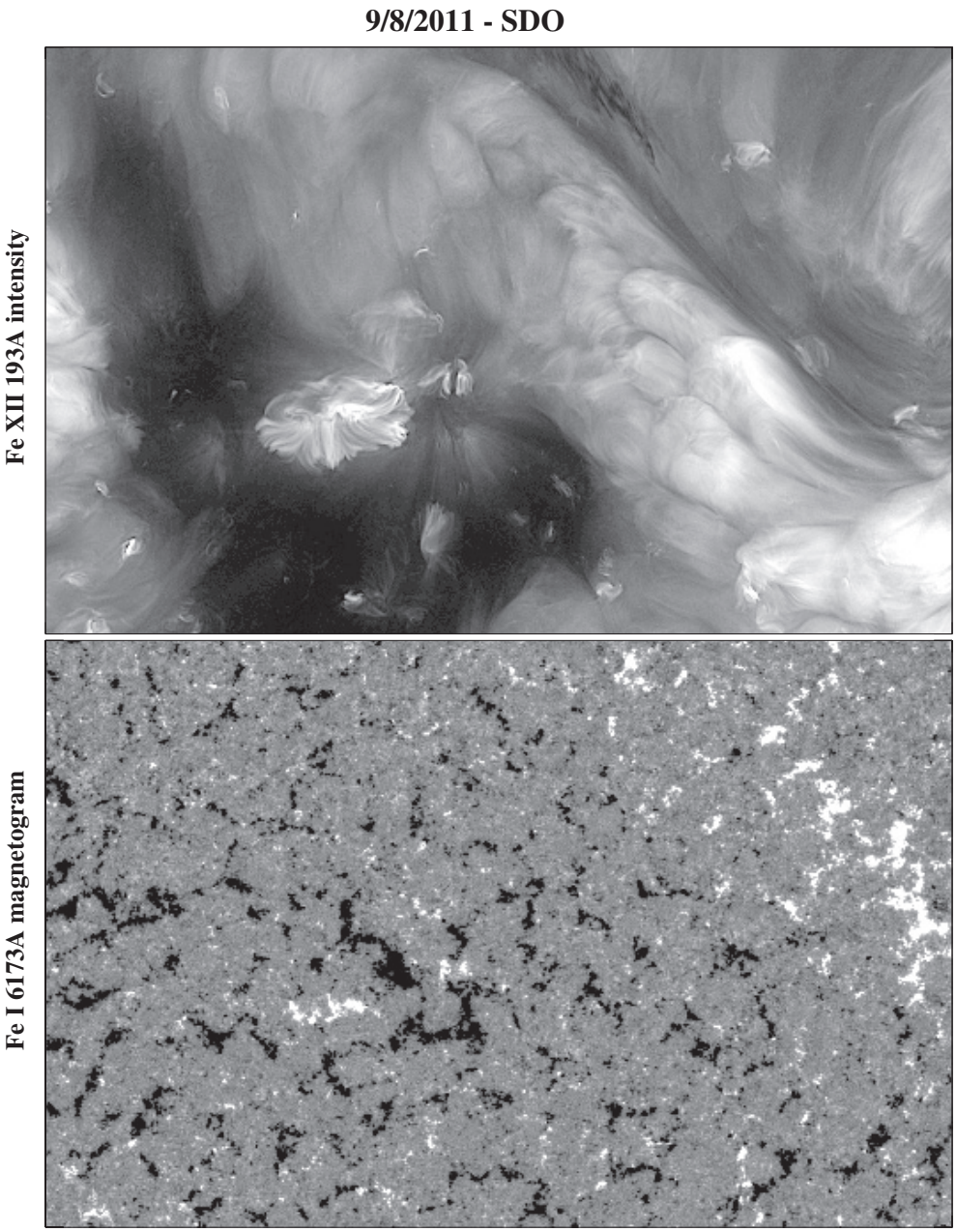

Figure 7. Blow-up of the region within the dotted box in Figure 6, comparing the region of coronal cells with an HMI photospheric magnetogram. In this example, the magnetic region is dominated by elements of negative (black) magnetic polarity. Again, the coronal cells are centered on the elements of majority polarity.

The fact that the cellular regions contain an appreciable amount of minority-polarity flux suggests a possible model for their magnetic geometry. In the Appendix, we consider a linear distribution of flux in which the majority polarity is concentrated in equal amounts at uniformly spaced (supergranular) intervals and the minority polarity is spread uniformly along the line. Figure 15 is a view of the resulting potential field lines for a minority- to majority-polarity flux ratio of 0.10 (top panel) and 0.30 (bottom panel). In these plots, the relatively strong flux concentrations "grab" the incipient field lines of the minority polarity before they can extend very far from the line, thereby causing the closed loops to lie close to the surface. These closed loops extend to slightly greater heights when the minority-polarity ratio is 0.30 than when it is 0.10, but even those higher loops lie in the chromosphere, within 0.4 of a supergranular radius from the surface where the field is non-potential. By comparison, Figure 3 suggests that the excess majority-polarity flux extends upward into the corona as a potential field that arches over the nearby filament channel to join distant regions of opposite polarity.

The disk observations of coronal cells might lead one to suppose that the cells are composed of closed loops that connect elements of minority-polarity flux to the nearby concentrations of majority-polarity flux. However, at the relatively low heights suggested by our calculations, these loops would not be visible as long, outward-projecting plumes as they approach the limb.

In addition, the minority-polarity flux is not distributed smoothly around the network concentrations of majority-polarity flux, which raises the question of why the dark lanes extend smoothly around the cells. If we were observing the tops of the closed field lines, we would expect to see an irregular distribution without such smooth boundaries between adjacent

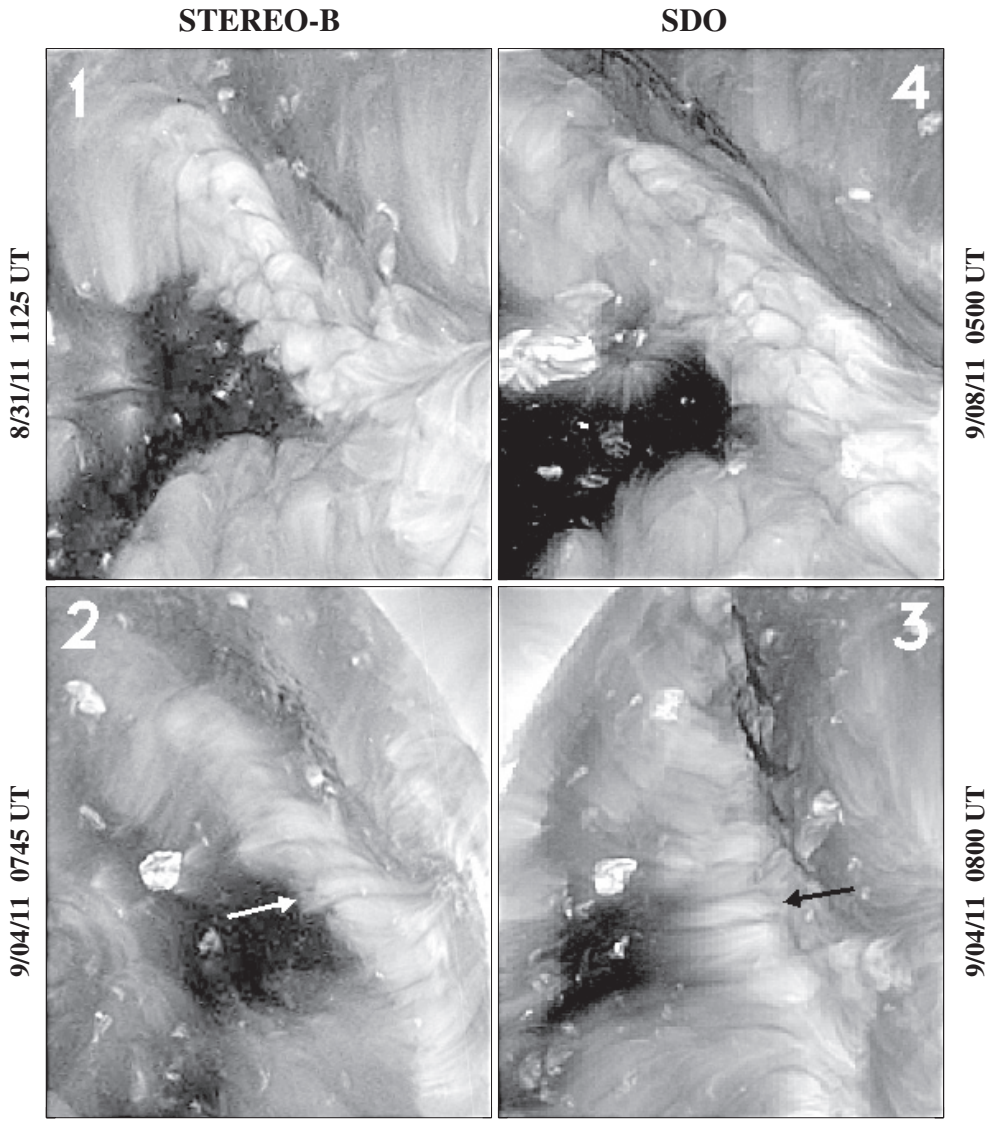

Figure 8. Same as in Figures 4 and 5, a clockwise progression from the upper left shows cells on the disk as seen from *STEREO-B*, turning to plumes projecting to the right in the oblique view 4 days later from *STEREO-B*, but projecting to the left in the simultaneous oblique view from *SDO*, and then turning back to cells again as seen closer to disk center on 2011 September 8 from *SDO*. The region must contain radial plumes like candles on a birthday cake, which are only visible as cells when they are seen from above.

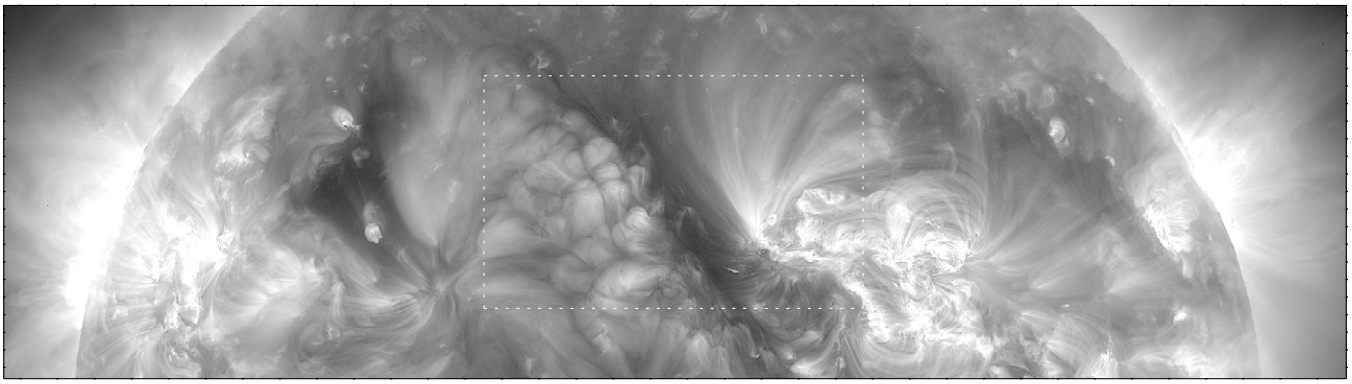

Figure 9. Fe XII 193 Å image from *SDO* on 2011 September 20, showing coronal cells lying east of a filament channel. This region of cells was created when a large coronal hole filled in during 2011 September 1–3 (as seen from *STEREO-A*), leaving the residual hole now visible slightly east of the cells. The box refers to the region shown in Figure 10.

cells. Evidently, the 1 MK emission originates from the much longer field lines that extend outward and upward from the concentrations of majority-polarity flux, and the cell boundaries occur where the field lines from the strong like-polarity sources encounter each other on their way outward like the field lines of pseudo-streamers (Wang et al. 2007).

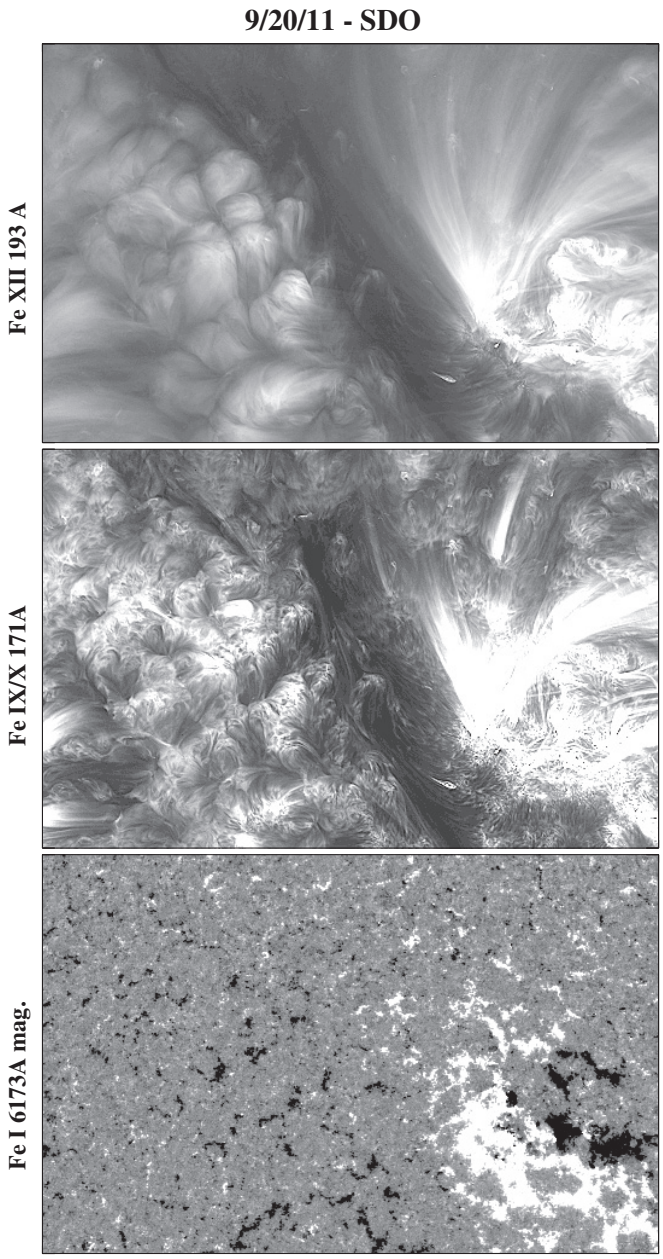

Figure 10. Blow-up of the region in Figure 9, comparing an Fe XII 193 Å image (top) with an Fe IX/X 171 Å image (middle), and an HMI magnetogram (bottom). In the relatively hot (1.2 MK) Fe XII line, the cells are centered on concentrations of majority-polarity flux. However, in the cooler (0.6 MK) Fe IX/X image, the cells lose their smooth character, and appear as a collection of small-scale fibrils similar to those seen in the chromosphere.

Reardon et al. (2011) have described "evidence for two separate but interlaced components of the chromospheric magnetic field" (p.1)—one component that remains in the chromosphere as a low-lying canopy of non-potential fields, and a much stronger component that extends into the corona as a potential field joining external regions of opposite polarity. Whereas Reardon et al. (2011) were observing the chromospheric component of the network field in their Ca II 8542 Å images, we are observing the coronal component in the Fe XII 193 Å images.

We have looked systematically at daily 193 Å images obtained with the *SDO* spacecraft, and found 12 examples during 2011 and two examples in 2010. Although the cells are also visible in 195 Å images obtained with the *STEREO* spacecraft, we are not aware of any examples during the quiet times near sunspot minimum in 2008–2009, prior to the launch of *SDO*. Presumably, this is related to the lack of strong regions of opposite-polarity flux nearby. Without such opposite-polarity flux, the cellular field lines would be open or very long, and the cells would be replaced by coronal holes or diffuse emission when observed in spectrum lines formed at 1 MK, and the accompanying filament channels would not exist. But during the previous sunspot cycle when solar activity was high and filaments were common, 195 Å images, obtained with the EIT instrument on *SOHO*, showed numerous cellular regions.

Thus, it is easy to imagine that the polar coronal holes are filled with magnetic plumes, most of which are "unlit" at sunspot minimum when nearby regions of opposite polarity are not present. Exceptions occur when ephemeral regions erupt in the holes to temporarily "light up" these magnetic structures to form polar plumes (Wang & Sheeley 1995; Wang et al. 1997a; Deforest et al. 1997; Wang 1998; Raouafi et al. 2008). However, during the rising phase of the cycle, active regions erupt at high latitude, producing enhancements of coronal intensity along the boundaries of the holes and filament channels along the associated neutral lines (Sheeley et al. 1989). In Fe XII 193 Å images, these enhancements consist of elongated features that extend upward along field lines that were created when expanding loops from the active region reconnected with open field lines of the coronal hole. Based on their plume-like geometry and their location between the polar coronal hole and the high-latitude filament channel, we suppose that these features are coronal cells, observed toward the polar limb. If so, then their cellular structure ought to be visible from high latitude.

During our analysis of the center-to-limb variation of the three cellular regions shown in Figures 1–11, we encountered several transient events, including three filament eruptions (2011 June 14, 2011 September 10, and 2011 October 22), and the closing of a large coronal hole during 2011 September 1–3. The June 14 filament eruption was seen simultaneously from *STEREO-B* and *SDO*, and seemed typical of these events. These observations showed the sudden evacuation of the cellular region, presumably associated with the transient opening of its closed field lines, and the reappearance of those same cells in the wake of the "flare ribbon" that subsequently moved across the evacuated area. Likewise, the more permanent closing of the coronal hole during September 1–3 was accompanied by the formation of the large cellular region shown in Figures 9–11. From these observations, it is clear that the cellular regions bear a close relation to the evolution of coronal holes, appearing when the holes close and disappearing when the holes open.

This raises the question of what keeps the cells visible, or, using the analogy of "candles on a cake," what keeps the candles lit. We have seen that the candles are lit when their majority-polarity flux is linked through the corona to its opposite-polarity counterpart in a large active region. The neighboring filament channel seems to be a sign of this connection, but with occasional interruptions when the filament erupts. However, the candles are not lit when the region lacks such a link, either because the field is open, or because the opposite-polarity field is too weak or too far away (as suggested by the lack of intensity enhancements at the edges of the polar coronal holes at sunspot minimum). This returns us to the idea that the enhanced heating occurs when the loops are short and rooted in strong fields—an idea that has been used previously (Wang et al. 1997b; Lean et al. 1999) to simulate the long-term variation of the Sun's coronal intensity.

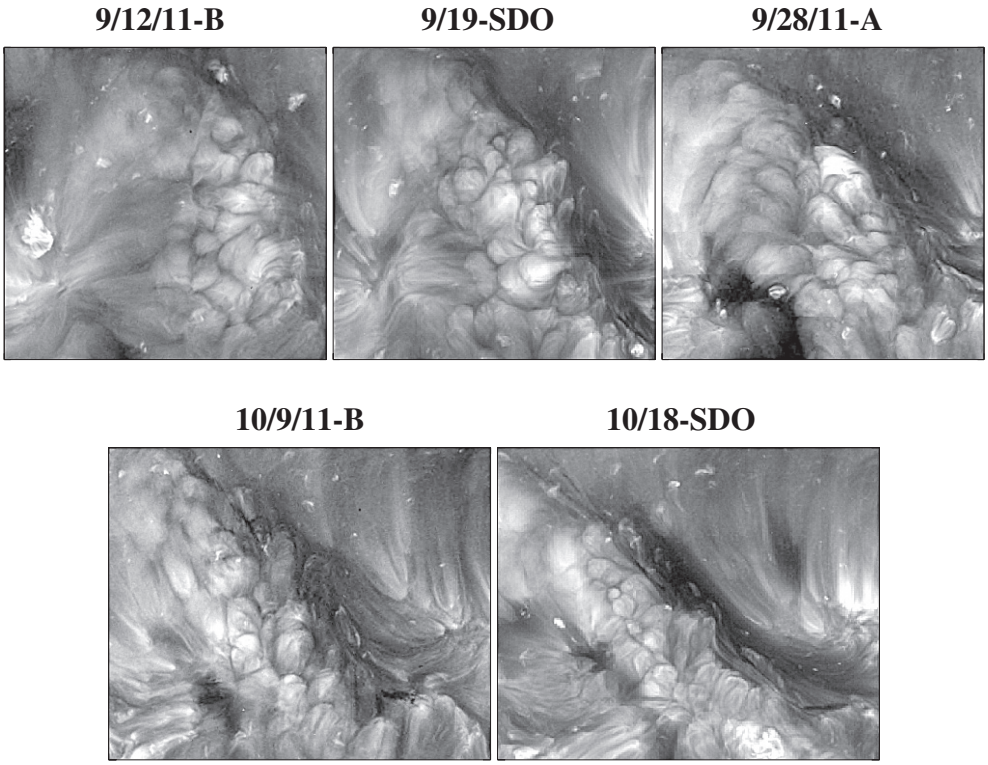

Figure 11. Cells of the previous two figures seen consecutively from *STEREO-B*, *SDO*, and *STEREO-A* during their disk passages in September and October of 2011. In the lower panels, the field of view has been extended eastward to show the trailing portion of the region as it became sheared by differential rotation.

We are grateful to Nathan Rich (NRL) for his continuing help in the development of software for observing and analyzing *SOHO*, *STEREO*, and *SDO* images. We are also grateful to J. W. Harvey (NSO) for useful discussions, including the suggestion to use the EIS spectra to construct a Dopplergram of the cellular field of view. *Hinode* is a Japanese mission developed and launched by ISAS/JAXA, with NAOJ as domestic partner and NASA and STFC (UK) as international partners. It is operated by these agencies in cooperation with ESA and NSC (Norway). We are grateful to the EIS science team for the use of its spectral observations. *SOHO* is a joint ESA–NASA program, and its EIT images were provided by the *SOHO* EIT Consortium. EUVI is part of the SECCHI instrument developed for the NASA *STEREO* mission. We are grateful to the SECCHI science team for providing the EUVI images and to the AIA and HMI science teams for providing observations from the NASA *SDO* spacecraft. Financial support was provided by NASA and the Office of Naval Research.

APPENDIX

MODELING THE FIELD-LINE GEOMETRY

Here, our objective is to derive the equations for the potential field whose field lines are plotted in Figure 15. Referring to Figure 16, we represent the network flux concentrations by equal amounts of positive flux, Φ, placed at equally spaced locations, $x_j = 2aj$, along the x-axis, where $j = 0, \pm1, \pm2, ...$, and a is the semi-network spacing, taken to be a supergranular radius. In addition, we represent the minority-polarity flux by a linear flux density, $-\sigma$, spread uniformly along the x-axis. We wish to evaluate the magnetic field at the point $P(x,y)$ due to all of these sources.

First, we consider the field due to the positive flux concentrations. For the jth source, the potential field is given by a simple inverse-square relation

$$\mathbf{B}_j^+ = \frac{\Phi}{4\pi r_j^2}\mathbf{e}_j = \frac{\Phi}{4\pi r_j^2}\frac{\mathbf{r}_j}{r_j} = \frac{\Phi}{4\pi r_j^3}(\mathbf{x}_j + \mathbf{y}_j), \tag{A1}$$

where $\mathbf{e}_j$ is a unit vector in the $\mathbf{r}_j$ direction, and $\mathbf{x}_j = (2aj+x)\mathbf{e}_x$ and $\mathbf{y}_j = y\mathbf{e}_y$. The quantities $\mathbf{e}_x$ and $\mathbf{e}_y$ are unit vectors in the x- and y-directions, respectively. Resolving these vectors into components along the x- and y-directions, and summing over all of the positive flux elements, we have

$$B_x^+ = \frac{\Phi}{4\pi}\sum_{j=-\infty}^{\infty}\frac{(2aj+x)}{[(2aj+x)^2+y^2]^{3/2}} \tag{A2}$$

and

$$B_y^+ = \frac{\Phi}{4\pi}\sum_{j=-\infty}^{\infty}\frac{y}{[(2aj+x)^2+y^2]^{3/2}}. \tag{A3}$$

Second, we consider the field due to the negative flux distribution. For this uniform linear distribution of flux, the field is independent of x and directed radially inward toward the axis. Consequently, its magnitude B_y^- can be determined directly from Gauss's Law, as applied to a cylinder of radius y and length Δx concentric with the x-axis. Equating the surface integral of the field to the flux inside the cylinder, we obtain

$$B_y^- 2\pi y\Delta x = -\sigma\Delta x. \tag{A4}$$

Solving for the field, B_y^-, we obtain

$$B_y^- = -\frac{\sigma}{2\pi y} = -\frac{\sigma a}{2\pi a^2(y/a)}. \tag{A5}$$

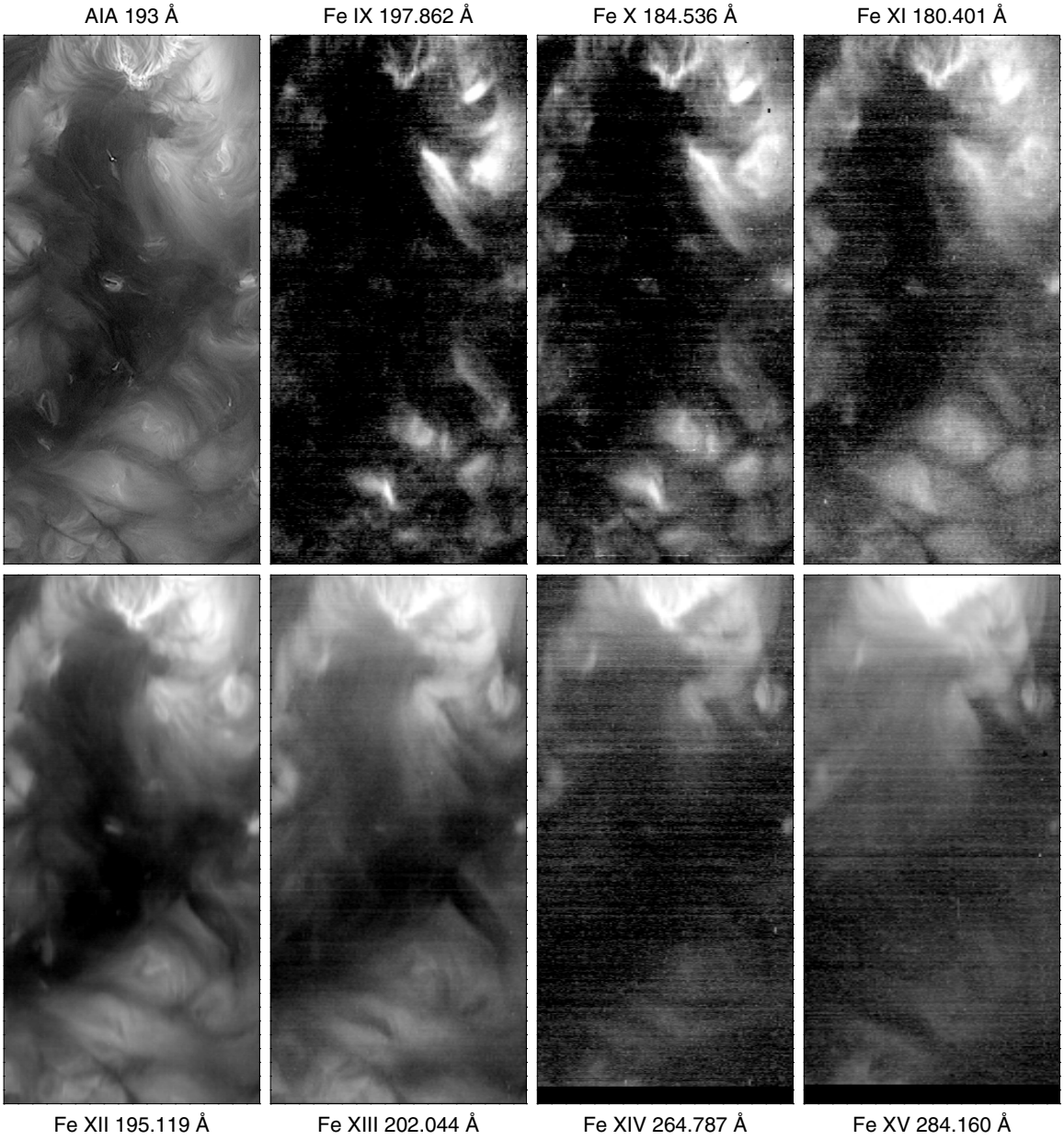

Figure 12. Comparison of an image, obtained with the AIA 193 Å filter (upper left), and a sequence of spectrally resolved images of the same area, obtained with the EIS instrument on *Hinode*. The cells along the southwest (lower right) boundary of the central coronal hole are most visible in the lines of Fe XI–Fe XII, corresponding to a temperature ~1.2 MK.

Combining the terms for the positive and negative flux distributions, and expressing x and y in units of a, we have

$$B_x(x, y) = \left(\frac{\Phi}{4\pi a^2}\right) \sum_{j=-\infty}^{\infty} \frac{(2j + x)}{[(2j + x)^2 + y^2]^{3/2}}, \quad \text{(A6)}$$

$$B_y(x, y) = \left(\frac{\Phi}{4\pi a^2}\right) \left[\sum_{j=-\infty}^{\infty} \frac{y}{[(2j + x)^2 + y^2]^{3/2}} - \frac{r}{y}\right], \quad \text{(A7)}$$

where the positive quantity $r = 2a\sigma/\Phi$ is the ratio of the amount of minority-polarity flux to the amount of majority-polarity flux. These are the equations that we used to calculate the field-line distribution in Figure 15.

It is instructive to determine the location of the neutral points of the field, and thereby to learn how far the closed loops can reach from the Sun's surface. For this purpose, we note that $B_x(x, y)$ vanishes whenever x/a is an odd integer. Consequently, we set $x = 1$, and determine y from the equation $B_y(1, y) = 0$. From Equation (A7), we obtain

$$\sum_{j=-\infty}^{\infty} \frac{y}{[(2j + 1)^2 + y^2]^{3/2}} - \frac{r}{y} = 0, \quad \text{(A8)}$$

which is equivalent to

$$y^2 \sum_{j=-\infty}^{\infty} \frac{1}{[(2j + 1)^2 + y^2]^{3/2}} = r. \quad \text{(A9)}$$

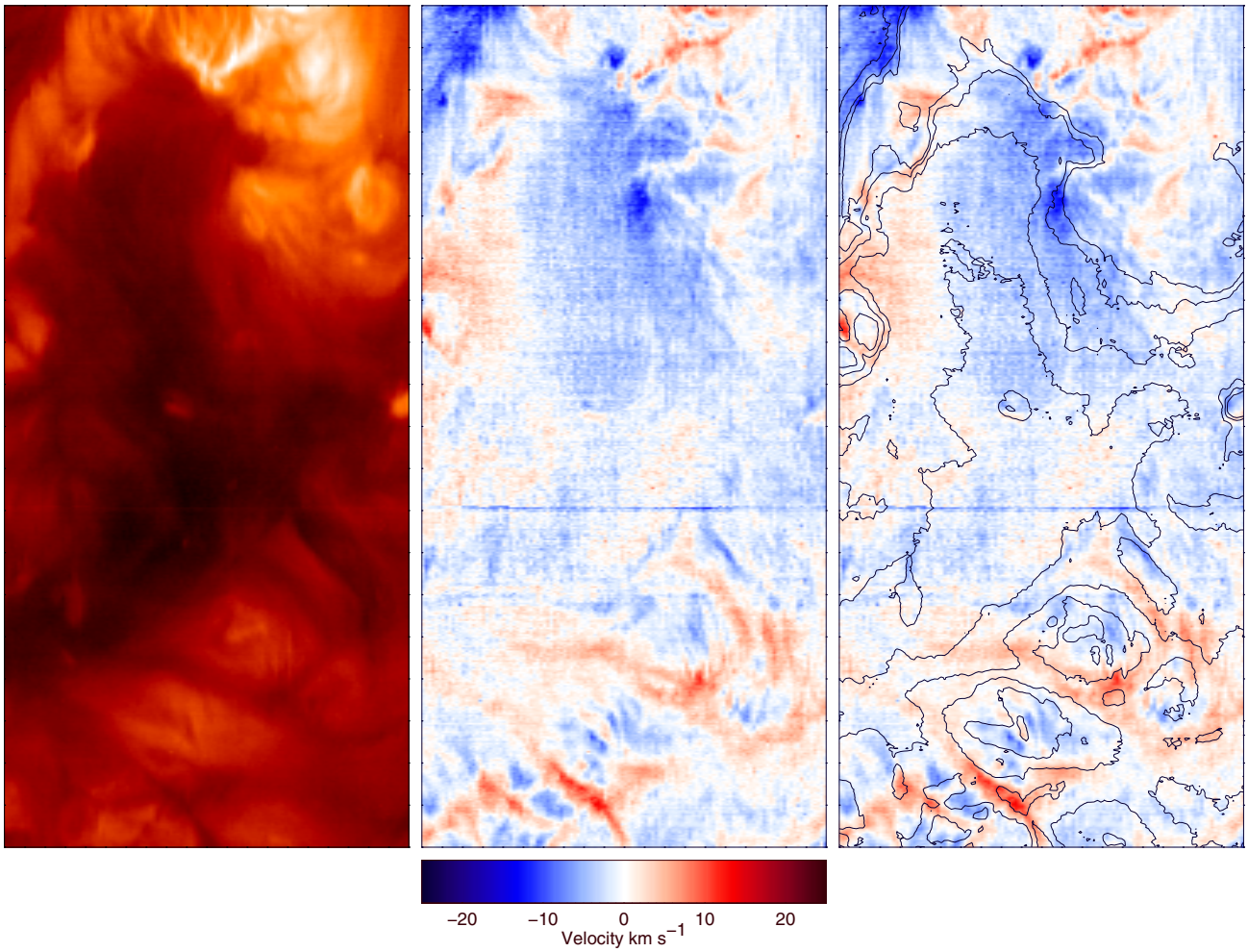

Figure 13. Center: an EIS Fe XII 193 Å Dopplergram, indicating the line-of-sight velocity field in the region shown in the previous figure, with blue indicating upward motions and red indicating downward motions relative to an arbitrary zero point. For comparison, the Fe XII intensity field is shown in the left panel and the intensity contours are superimposed on the Doppler field in the right panel. Narrow lanes of red coincide with the boundaries of the cells, indicating downward motions relative to the cell centers and the coronal hole.

(A color version of this figure is available in the online journal.)

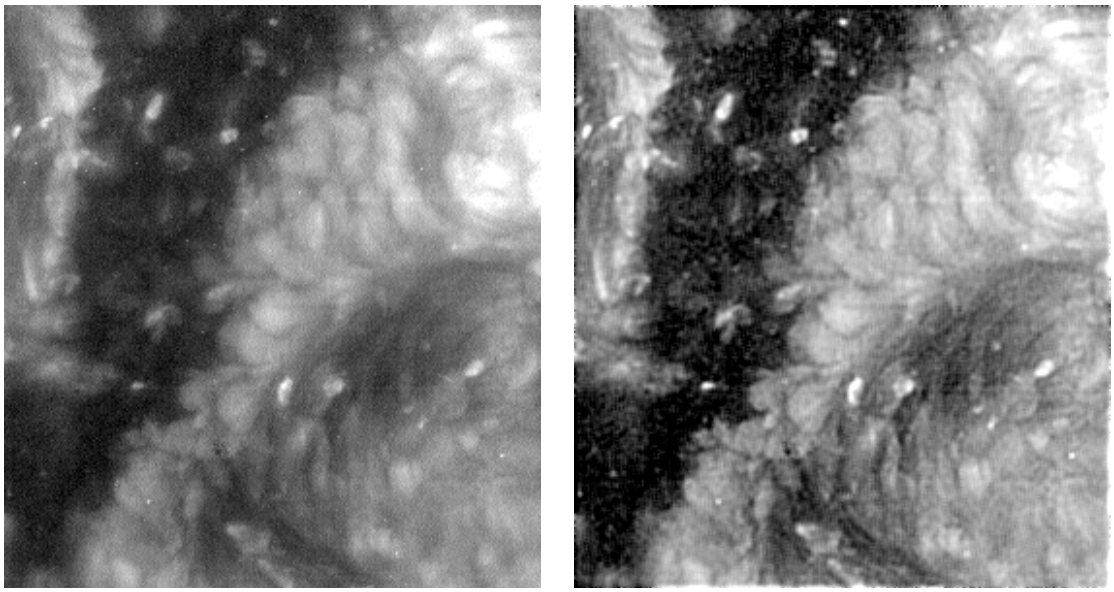

Figure 14. Two versions of an Fe XII 195 Å image obtained with the EIT instrument on *SOHO* on 2000 December 6, showing cells with (right) and without (left) sharpening. Again, the region of cells is centered between a coronal hole (left) and a filament channel (right).

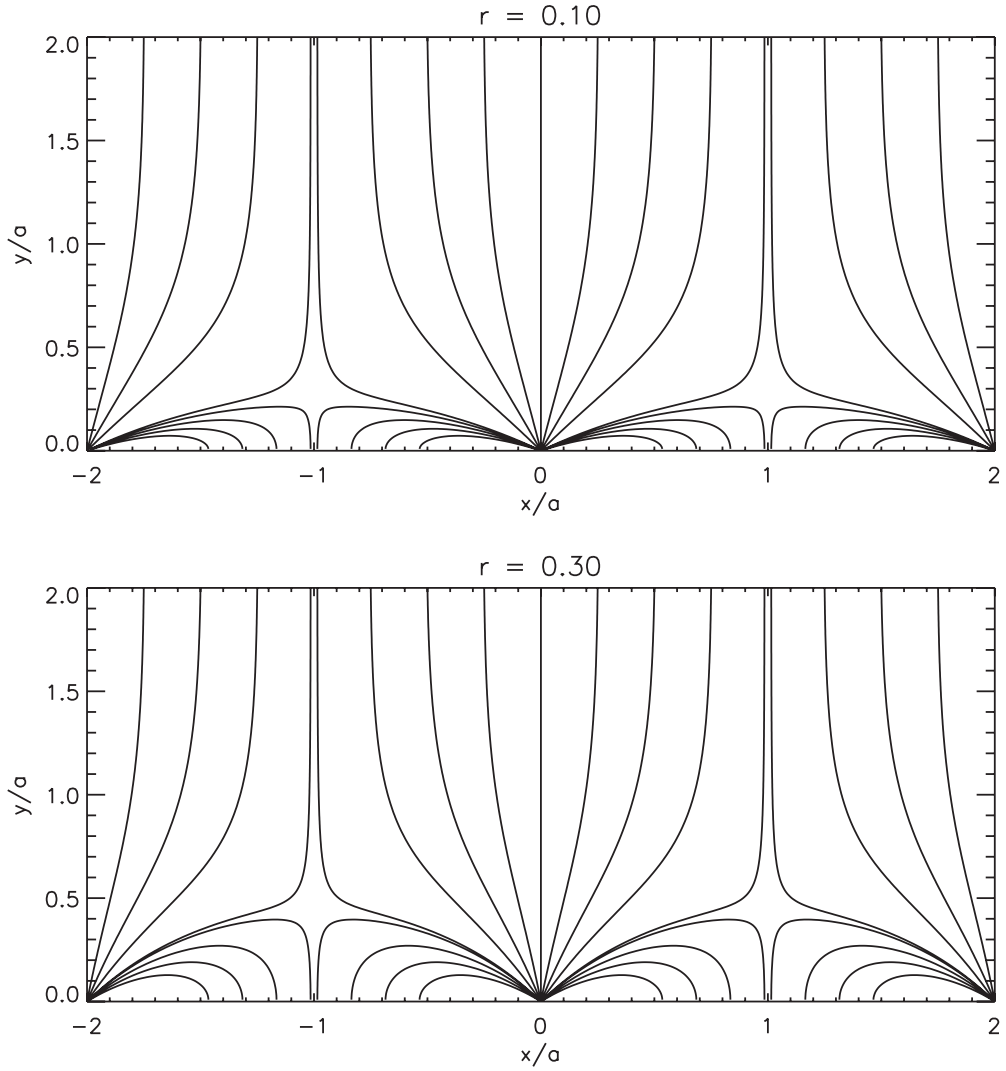

Figure 15. Potential field lines for an axially symmetric model in which identical concentrations of positive flux are distributed at even integers along the x-axis and a smaller amount of negative flux is distributed uniformly along the axis. The ratio, r, of negative to positive flux is 0.1 in the upper panel and 0.3 in the lower panel, corresponding to the range of values measured in the cell regions of this paper. The closed loops lie closer to the surface when the amount of minority flux is smaller (upper panel) than when it is larger (lower panel).

For $y \ll 1$, Equation (A9) reduces to

$$2\sum_{j=0}^{\infty}\frac{1}{(2j+1)^3}y^2 = r. \tag{A10}$$

Because the sum in Equation (A10) is approximately 1.05, we finally obtain the approximate relation

$$y = \sqrt{\frac{r}{2.10}} \sim \sqrt{\frac{r}{2}}, \tag{A11}$$

where y is in units of the supergranular radius, a, and r is the minority- to majority-polarity flux ratio, $2a\sigma/\Phi$.

Thus, even for a value of r as large at 0.5, we would obtain $y \sim 0.5a$, which means that the height of the neutral point would be only half a supergranular radius, or about 7500 km above the Sun's surface. For more realistic values of r in the range 0.1–0.3, the height of the neutral point would be 0.2–0.4 supergranular radii, or 3000–6000 km above the surface. Consequently, the closed loops must lie in the chromosphere where the field is not potential.

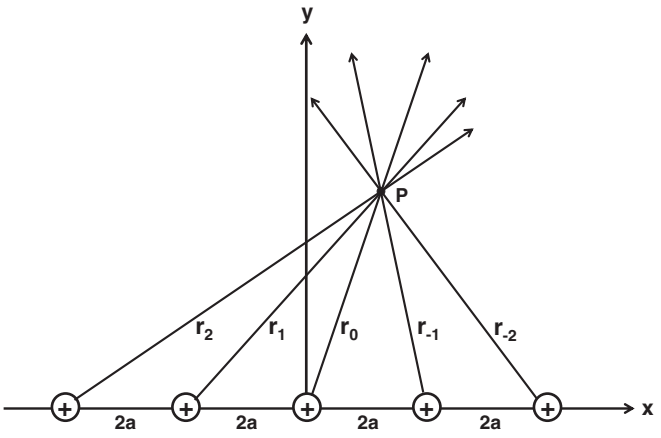

Figure 16. Sketch of the model used for deriving the field lines in Figure 15. Flux concentrations of equal strength are spaced at intervals, $2a$, along the x-axis, but only five of them are shown here. Each source produces an inverse-square radial field at the point P; their sum gives the total field due to the positive flux. As described in the Appendix, this field is then added to the field from a uniform distribution of negative-polarity flux along the x-axis to obtain the field whose lines are plotted in Figure 15.

REFERENCES

Culhane, J. L., Harra, L. K., James, A. M., et al. 2007, Sol. Phys., 243, 19
Deforest, C. E., Hoeksema, J. T., Gurman, J. B., et al. 1997, Sol. Phys., 175, 393
Delaboudinière, J.-P., Artzner, G. E., Brunaud, J., et al. 1995, Sol. Phys., 162, 291
Domingo, V., Fleck, B., & Poland, A. I. 1995, Sol. Phys., 162, 1
Doschek, G. A., Mariska, J. T., Warren, H. P., et al. 2007, ApJ, 667, L109
Feldman, U., Widing, K. G., & Warren, H. P. 1999, ApJ, 522, 1133
Feldman, U., Widing, K. G., & Warren, H. P. 2000, ApJ, 529, 1145
Howard, R. A., Moses, J. D., Vourlidas, A., et al. 2008, Space Sci. Rev., 136, 67
Lean, J. L., Wang, Y.-M., Mariska, J. T., & Acton, L. W. 1999, BAAS, 31, 987
Lemen, J. R., Title, A. M., Akin, D. J., et al. 2012, Sol. Phys., 275, 17
Raouafi, N.-E., Petrie, G. J. D., Norton, A. A., Henney, C. J., & Solanki, S. K. 2008, ApJ, 682, L137
Reardon, K. P., Wang, Y.-M., Muglach, K., & Warren, H. P. 2011, ApJ, 742, 119
Schou, J., Scherrer, P. H., Bush, R. I., et al. 2012, Sol. Phys., 275, 229
Sheeley, N. R., Wang, Y.-M., & Harvey, J. W. 1989, Sol. Phys., 119, 323
Simon, G. W., & Leighton, R. B. 1964, ApJ, 140, 1120
Wang, Y.-M. 1998, ApJ, 501, L145
Wang, Y.-M., & Sheeley, N. R., Jr. 1992, ApJ, 392, 310
Wang, Y.-M., & Sheeley, N. R., Jr. 1995, ApJ, 452, 457
Wang, Y.-M., Sheeley, N. R., Jr., Dere, K. P., et al. 1997a, ApJ, 484, L75
Wang, Y.-M., Sheeley, N. R., Jr., Hawley, S. H., et al. 1997b, ApJ, 485, 419
Wang, Y.-M., Sheeley, N. R., Jr., & Rich, N. B. 2007, ApJ, 658, 1340
Warren, H. P., Ugarte-Urra, I., Young, P. R., & Stenborg, G. 2011, ApJ, 727, 58
Young, P. R., O'Dwyer, B., & Mason, H. E. 2012, ApJ, 744, 14